Progress in Readout Electronics for STCF ECAL

Hanlin Yu, Zhongtao Shen, Yue Long, Yunlong Zhang, Zekun Jia, Yong Song, Shubin Liu

Abstract—**The Super Tau-Charm Facility (STCF) is a significant initiative for accelerator-based particle physics in China. Electromagnetic Calorimeter (ECAL) is one of the important detectors of STCF, which is tasked with the precise measurement of photons. STCF ECAL employs pure Cesium iodide (pCsI) as its scintillation crystal and uses a large-area avalanche photodiode (APD) as a photoelectric conversion device. This paper explores the methods for energy and time measurement, as well as signal processing under high event rates. The readout electronics scheme, which combines a charge-sensitive amplifier (CSA) with a waveform fitting algorithm, is experimentally verified. Measurements indicate that the energy measurement noise is 0.8 fC, and the time measurement accuracy reaches 300 ps at 1 GeV.**

Index Terms—**Readout Electronics, STCF ECAL, APD, CSA, Waveform Fitting**

I. INTRODUCTION

SUPER Tau-Charm Facility (STCF) is a significant initiative for accelerator-based particle physics after Beijing Electron-Positron Collider (BEPC-II) in China [1]. The design collision brightness of STCF is greater than $0.5 \times 10^{35} \cdot cm^{-2} \cdot s^{-1}$, and the collision centroid energy reaches 2-7GeV. The operation of the STCF will provide a unique platform for the study of tau-charm physics and hadron physics.
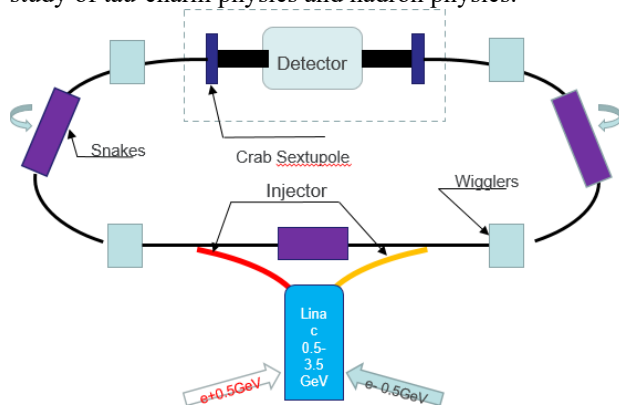

Fig. 1. Architecture of Super Tau Charm Facility (STCF)

Electromagnetic Calorimeter (ECAL) is one of the important detectors of STCF, which is tasked with the precise measurement of photons. In the face of a complex background environment, STCF ECAL needs to obtain accurate energy information and time information of photons at the same time to effectively suppress the background, so compared with traditional electromagnetic energy generators, STCF ECAL puts forward higher requirements for time resolution [2].

As is shown in Fig. 2, STCF ECAL selects pure Cesium iodide (pCsI) with the advantages of fast response speed and good anti-irradiation performance as its scintillation crystal [3,4] and uses a large-area avalanche photodiode (APD) [5,6,7] with a certain internal gain as a photoelectric conversion device to make up for the shortcomings of low pCsI optical yield. Therefore, readout electronics need to be designed with low noise to meet the measurement needs of STCF ECAL.
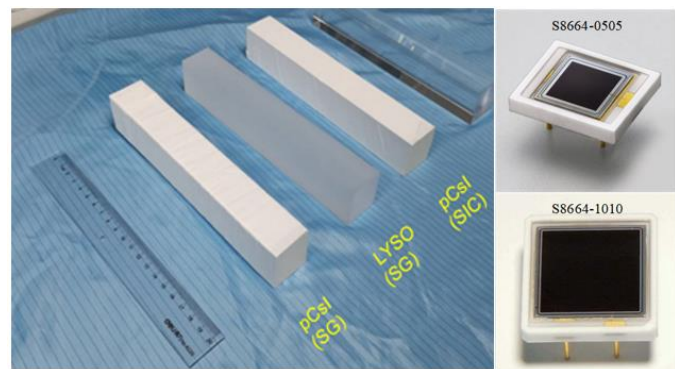

Fig. 2. pCsI Crystal and APD

The main function of readout electronics is to measure the signals of APDs. According to the simulation, the range of deposition energies on a single crystal is 3 MeV - 3 GeV. Assuming a photoelectric yield of 100 p.e./MeV for pCsI and a 50-fold multiplication gain achieved by the APD at normal operating voltage, the fluorescence converted by the APD ranges from 2.4 fC to 2.4 pC, which means the noise must be lower than 2.4/3 = 0.8fC.

STCF ECAL includes 6732 barrels, 1938 end caps, the readout electronic noise reaches less than 1MeV, the temporal resolution reaches 200ps at 1GeV (3000fC), the sub-nanosecond order at 100MeV (300fC), the background event rate can reach 1.5MHz. Besides, to realize the distinction between neutral hadrons and photons, 300 ps time resolution at 1 GeV; and sub-nanosecond time resolution at 100 MeV is achieved.

Hanlin Yu, Zhongtao Shen, Yue Long, Yunlong Zhang, Zekun Jia, Yong Song and Shubin Liu are with State Key Laboratory of Particle Detection and Electronics, and Department of Modern Physics, University of Science and Technology of China, No.96, Jinzhai Road, Hefei, 230026, China (e-mail: henzt@ustc.edu.cn).

II. ELECTRONIC DESIGN

A. Energy Measurement

The Front-End Module (FEM) of the readout electronics uses a CSA-based measurement scheme. Due to the large APD junction capacitance (270 pF) and high leakage current, one or more JFETs are used as the input stage to mitigate these effects. Fig. 3 illustrates the circuit containing the CSA and APDs.
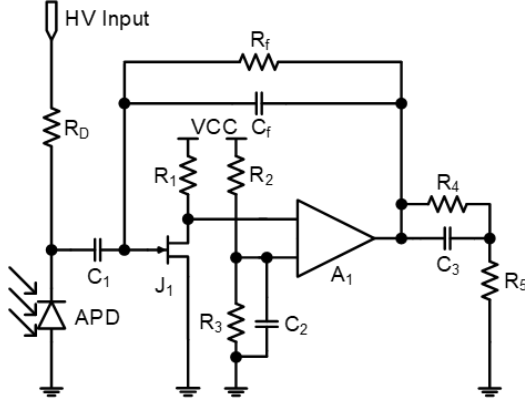
Fig. 3. Charge Sensitive Amplifier Schematic

After analyzing the circuit, the noise can be classified as I_{parrel} and V_{series}, the voltage noise in series can be converted into current noise in parallel by the following formula:

$$I_{series-equ}^2 = V_{series}^2(\omega C_{\Sigma}^2)$$

Where $\omega = 2\pi f$, $C_{\Sigma} = C_{APD} + C_{JFET} + C_f$, The noise after CSA and CR-RC^2 shaping circuit can be described as the following equation [8]:

$$V_{nout}^2 = \int_0^{+\infty} |H(\omega)|^2 \cdot (I_{parallel}^2 + I_{series-equ}^2) df$$

$$= \frac{3\tau}{32C_f^2} \cdot I_{parallel}^2 + \frac{C_{\Sigma}^2}{32C_f^2\tau} \cdot \left(\frac{8kT}{3g_m} + \frac{4kT(R_1 + R_2 + R_3) + V_{nOP}}{g_m^2 R_1^2}\right) + \frac{A_f C_{\Sigma}^2}{4C_f^2}$$

The circuit structure of the RC^2 shaping network is shown in Fig. 4, and the time constant after the pole-zero phase cancellation is equal to the RC^2 shaping time.
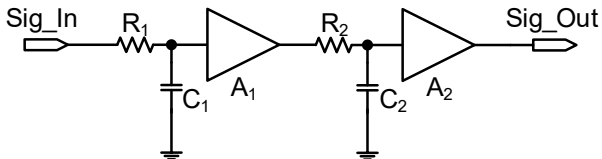
Fig. 4. Schematic diagram of RC2 shaping circuit

It can be seen that the larger the JFET transconductance, the lower the noise. To get a good noise performance, 2SK715 with a transconductance up to 50 mS, is selected. Besides, the equivalent saturated drain current can be increased by connecting multiple JFETs in parallel to improve the g_m. In this paper, a scheme with three 2SK715s connected in parallel is used.

There is another key parameter in the CSA system that affects the noise - forming time, after calculation and analysis, in order to obtain the best system noise, the shaping time is determined to be 100ns.

The actual measurement of noise was carried out by connecting four S8664-1010 APDs to FEMs, and the system noise test results obtained are shown in Fig. 5, which shows that for high-gain channels, the filter forming process generally reduces the system noise by about 30%, and the equivalent noise charge of the signal after all channels are formed is not

more than 0.8 fC. For the low-gain channel, as in the case of electronic noise, the equivalent noise of the signal increases after forming due to the predominance of the noise introduced by the ADC's nonlinearity error, and the noise does not exceed 2.2 fC for all low-gain channels.
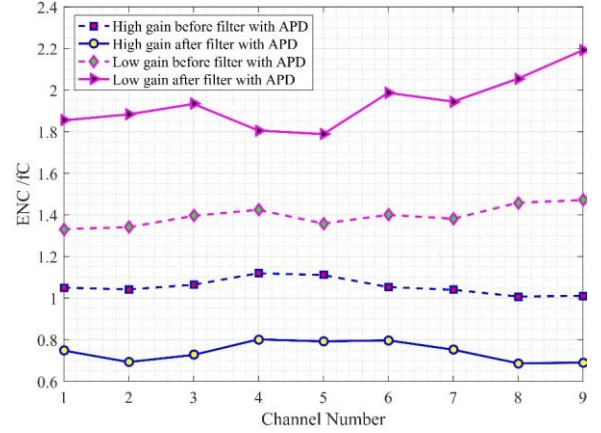
Fig. 5. Equivalent noise of the FEMs after APD is connected

It is obvious that the smaller the integration capacitance used in the CSA, the smaller the impact of the backstage noise of the overall noise, on the other hand, the CSA's integrated capacitance selection is relatively small, therefore the APD's capacitance and Miller capacitance are negligible for the CSA input.

There are two paths for the charge at the input end of the CSA, one path is through the APD to the ground, and the other path is through the CSA, which is shown in Fig. 6. The Miller capacitance C_{Miller} in the diagram can be represented as an equation:

$$C_{Miller} = |A|C_f$$

Where A is the amplification factor of the CSA circuit JFET and the op amp in Fig. 3, and C_f is the feedback capacitance (also known as integral capacitance).
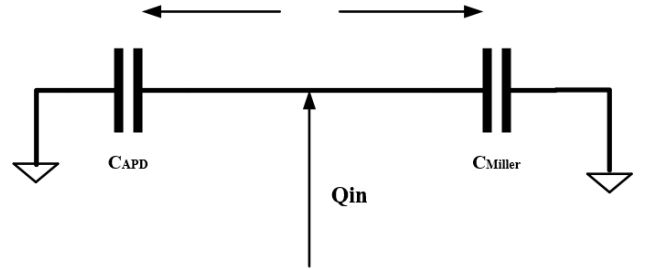
Fig. 6. The direction of the flow of charge

Since the CSA integral capacitance selected in this design is relatively small, and the corresponding Miller capacitance is also relatively small, the partial charge effect of the APD capacitor may not be negligible, in order to confirm the influence of this part on the energy measurement, LTSpice is used for simulation, and the input terminal adopts the impulse response signal, The effect of APD capacitance on the CSA output signal under different integrated capacitors is observed, and the simulation results are shown in Fig. 7. It can be seen that the smaller the integrated capacitance used, the greater the attenuation of the resulting signal.
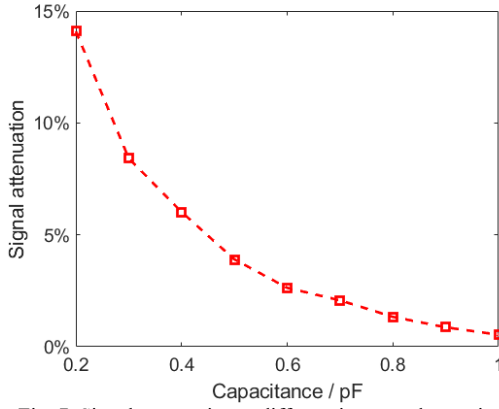
Fig. 7. Signal attenuation at different integrated capacitances

B. Timing Measurement

The waveform fitting algorithm is derived from the Belle II calorimeter upgrade electronics [9]. Sampling points are fitted by a template $F(t) = Af(t + \tau) + p$ by minimizing the chi-square as shown in the equation [10]:

$$\chi^2 = \sum_{i,j} (y_i - Af(t_i + \tau) - p) \, S_{ij}^{-1} \, (y_j - Af(t_j + \tau) - p)$$

Where $f(t)$ is the template shape function, A is the signal amplitude to be measured, τ is the signal arrival time, p is the actual pedestal, y_i is the signal amplitude at t_i, $S_{ij} = \overline{(y_i - \overline{y_i})(y_i - \overline{y_i})}$ is the noise covariance matrix. By least squares derivation, the information about A and τ can be obtained and the time error introduced by the sampling point noise can be obtained as shown in the equation:

$$\sigma_{t-n} \approx \frac{\sigma}{A\sqrt{\sum f'(t_i)}}$$

According to the above equation, it can be seen that in addition to the sampling noise, the slope of the waveform at the sampling point is also a major factor affecting the time resolution, and the rise time of the output waveform is affected by the bandwidth of the CSA circuit. Different CSA parameters will affect the bandwidth of the CSA, and the simulation results are shown in Fig. 8 by using LTSpice to observe the effect of APD capacitance on the rise time of the CSA output signal under different integrated capacitances. It can be seen that the smaller the integrated capacitance employed, the greater the rise time of the output signal of the CSA. The smaller the capacitance, the more pronounced the above effect is.
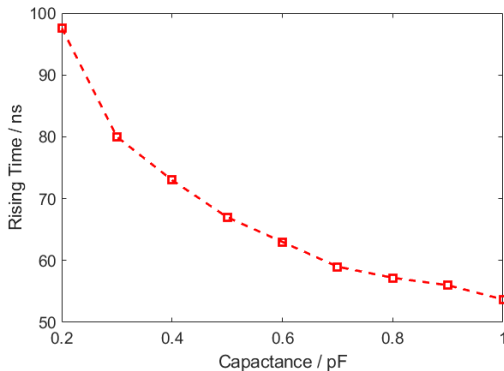

Fig. 8. Rising time at different integrated capacitances

According to the results of Fig. 7 and Fig. 8, 0.5pF is finally selected as the integrating capacitance for the CSA circuit.

Using the same SPM to measure multiple FEMs, the intrinsic time interval on the hardware between different FEMs is used as an observation, and the system's measurement accuracy of this time interval is used to reflect the timing accuracy of the waveform fitting. The Experimental Block Diagram is shown in Fig. 9.
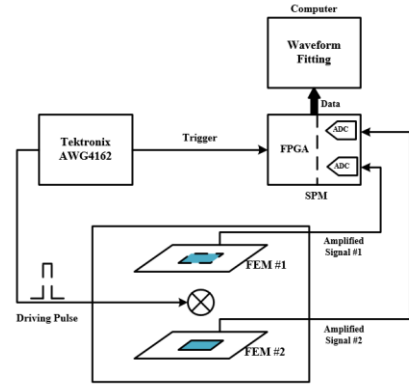

Fig. 9. Block diagram of the time measurement

At a charge of 200 fC (equivalent deposition energy of 1 GeV), the timing accuracy is about 165 ps; after the input signal charge is greater than 400 fC, the time measurement error of the system is less than 100 ps. The experimental results are shown in Fig. 10, after connecting the S8664-1010 APD, the timing accuracy of the waveform fitting method can meet the experimental requirements.
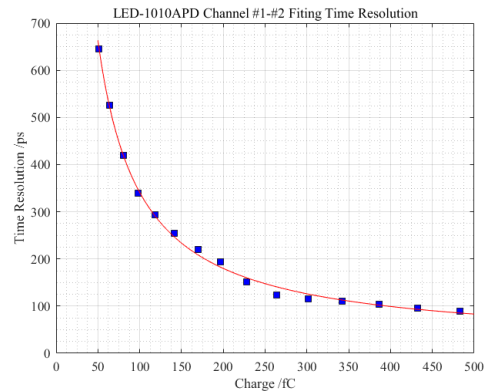

Fig. 10. Time Measurement Result

C. High Event rate Analysis

According to the results of the theoretical simulation of the working group [11], the ECAL single crystal will receive the rate of the background events of about 1.5 MHz; Meanwhile, the energy distribution of the background events is overwhelmingly concentrated in the low-energy interval of less than 1 MeV. In this regard, in order to evaluate the impact of this background on the above measurement scheme, the signal buildup is further analyzed in the following. According to the energy distribution of the background events and the average event rate, the probability that the background events with different energies appear within the CSA waveform width (700 ns) is estimated, and the results shown in Fig. 11 are obtained. From the calculation results, it can be seen that the probability of the occurrence of backgrounds with energies of 1 MeV and below within the waveform width is about 65%, and further, the probability of the occurrence of two and more events of such backgrounds within this range is about 28%; for the events of

backgrounds with slightly larger energies, e.g., 10 MeV, the probability of the occurrence of one and more events under the same conditions is about 0.6%, and the probability of the occurrence of two and more events at the same time falls to about 0.6%. The probability of one or more events under the same conditions is about 0.6%, while the probability of two or more events at the same time decreases to about 2×10^{-5}; for events with higher energies, the probability of their occurrence will be further reduced.
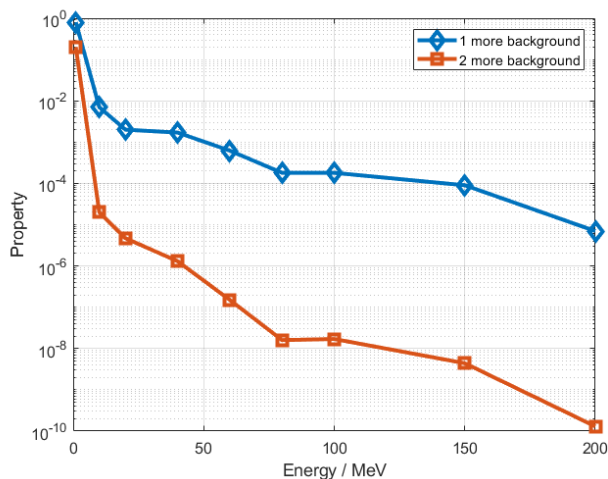

Fig. 11. Probability of different events of energy background within the width of a CSA waveform

Fig. 12 shows the probability of a background (10 MeV) exceeding the threshold in different time windows from the start point of the physical case, with the absolute probability on the left and the conditional probability on the right for the background to occur within the waveform width. The results show that the probability of background occurrence is directly proportional to the time width, and about 10% of all the backgrounds occur when the time difference between the background and the physical case is less than 70 ns, and the remaining 90% are events with a larger time interval.
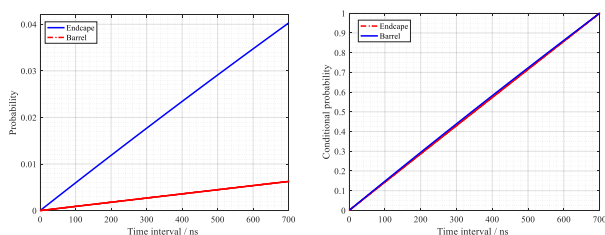

Fig. 12. The probability of a background over the threshold
(Left: Absolute; Right: Conditional)

According to the previous analysis of the energy and event rate of the background, the background with slightly larger energy and able to exceed the threshold, has a certain stacking probability with the physical signals, but the number of stacking is only one, and the probability of stacking of two or more signals will be reduced by two orders of magnitude compared to that of the stacking of two or more signals. Since there are at most two signals in each sampling time window, considering that multi-waveform fitting is more resource-consuming, the number of fitting points is reduced by calculating one by one to achieve the purpose of reducing the amount of computation, and the amplitude and time information of the first waveform is obtained by single fitting, and then this first waveform is

subtracted according to the shape of the waveform within the time window, and then thereafter the waveforms are fitted to the rest of the data, and the correct amplitude information and time information of the stacked signals can be obtained. The correct amplitude and time information of the stacked signal is obtained. The calculation flow is shown in Fig. 13.
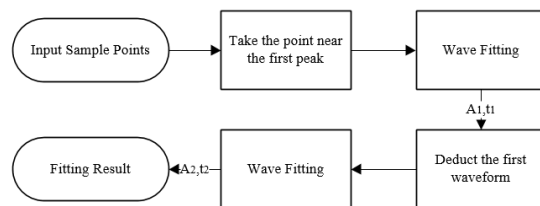

Fig. 13. Computational Flow for Processing Pile-up Signals

III. BACKGROUND SIGNAL SIMULATION PLATFORM

To verify the processing capability of the readout electronics for high event rate signals, a high background simulation verification experiment based on LEDs is designed. The verification experiment is based on the energy distribution and time distribution of the background obtained from the simulation, and samples are generated to produce background events containing time and energy information, and the sampling results are utilized to generate the corresponding signals to drive the LEDs to emit light, which in turn simulates the background situation in the experiment.

To validate the operation of the detection system in an actual background environment, this paper utilizes one LED to emit light to simulate the fluorescence produced by background particles, and another LED with fixed light intensity to simulate the fluorescence produced by physical events. By measuring the light signal representing the physical events, the effect of the background on the signal measurement can be assessed, as well as the effect of readout electronics on the suppression of high event rate backgrounds. Fig. 14 illustrates the LED driver circuit, which converts the drive voltage into the drive current through resistors, and the op-amp and BJT can provide isolation and drive.
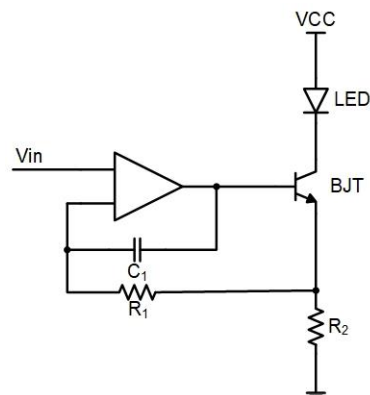

Fig. 14. LED driver circuit

The experimental platform for simulating background events using LEDs is shown in Fig. 15. A series of energy points are sampled by using the background energy distribution obtained by simulation, the time interval of adjacent background events is sampled, and a waveform used to drive the LED is generated, which is output by an arbitrary waveform generator AWG4162

used to simulate the background case, and the other LED emits a light signal with a fixed light intensity to simulate the actual physical signal.
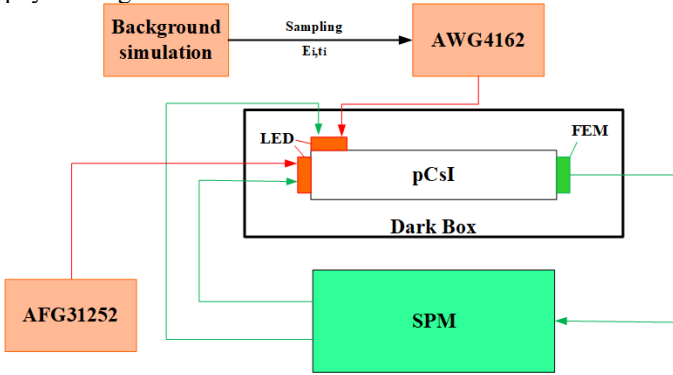

Fig. 15. LED background simulation test platform

The energy distribution of the partial background impulse sequence (time length 1 s) used in this experiment is shown in Fig. 16, which shows that the number of background events is close to 2×10^6 in a time window of 1 s, which is consistent with the event rate; the energy of the background events is mostly concentrated within 1 MeV, which is also consistent with the energy distribution of the background.
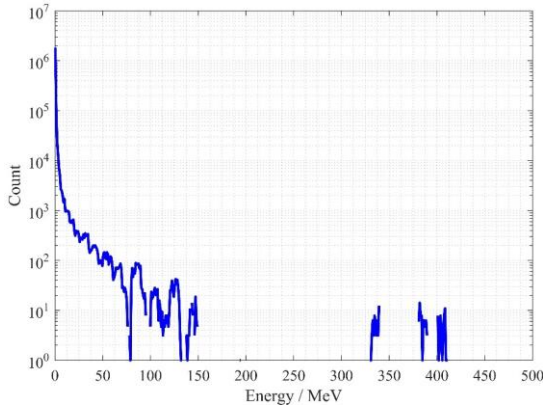

Fig. 16. Energy distribution of the background impulse sequence (in 1s)

Fig. 17 illustrates the superposition of these waveforms. As can be seen from the Fig., the first half of the waveform is mainly concentrated near the baseline; At the same time, this region is accompanied by a small number of energetic background waveforms, which are randomly distributed in time. Similarly, in the second half of the diagram, the shape of the physical case signal is clearly visible, and the background signal is also randomly superimposed on the physical case signal.
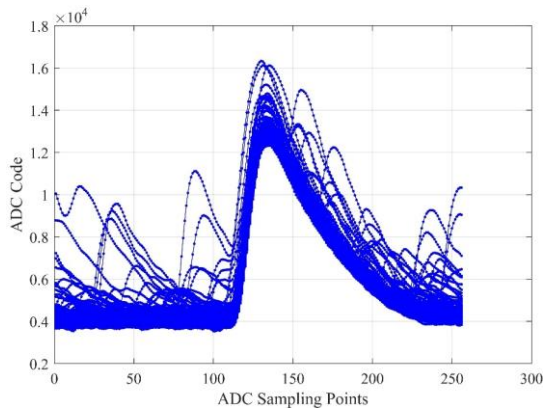

Fig. 17. Several waveforms in the presence of a background signal

The LEDs that simulate the physics case are driven all the time so that the signal to be measured in the acquired waveform is always there. Controls the LED drive or off of the analog background, simulating scenarios where the background signal is present and absent. According to the data acquisition method in Fig. 18, the waveforms with and without background signals are collected, and these waveforms are sent to the waveform fitting module, and the corresponding baseline, amplitude, and other information are obtained by fitting.
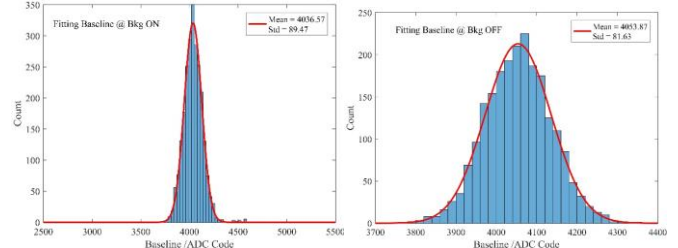

Fig. 18. The baseline distribution obtained by the waveform fitting before and after adding the background

The measurement results show that the presence or absence of background events has no obvious effect on the fitting results of the baseline, and the fluctuation of the background is less than 0.1 fC according to the standard deviation obtained by fitting the chart.

IV. COSMIC RAY TEST

The cosmic ray particles received by the detection unit are mainly muons produced by the clustering of primary cosmic rays in the atmosphere. These muons are in the energy interval with the lowest average ionization energy loss and belong to the minimum ionized particles (MIP). The MIP is utilized to pass through pCsI crystals and deposit energy, which is about 30 MeV for crystals with a thickness of about 6 cm. Measurement of the fluorescence signal at this energy allows verification of the operational status and performance of the detector unit as well as the readout electronics. The experimental block diagram of the cosmic ray MIP deposition energy spectrum test is shown in Fig. 19.
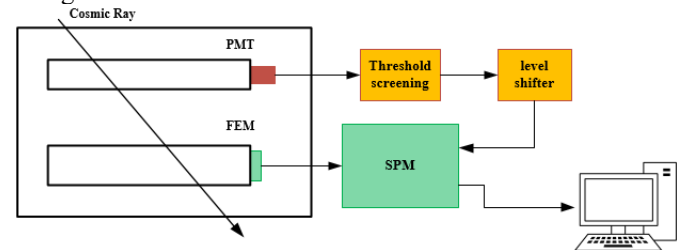

Fig. 19. The cosmic ray MIP deposition energy spectrum test

After about 12 hours of testing, a total of 15,344 instances were captured by the cosmic ray experiment, and the corresponding MIP deposition energy spectrum is shown in Fig. 20. From the Fig., it can be seen that the MIP peaks are about 6000 ADC code values and the baseline is about 1000 ADC code values, and the baseline and MIP peaks are separated obviously. Based on the electronics gain of the channel, it can be converted to obtain the MIP signal corresponding to a charge of about 37 fC. From this, the fluorescence yield of the detection unit is about 155 p.e./MeV, which is about 50% higher compared to the theoretical target of 100 p.e./MeV. The

noise of the system is no greater than 0.8 fC, corresponding to an equivalent noise energy of less than 649 keV.
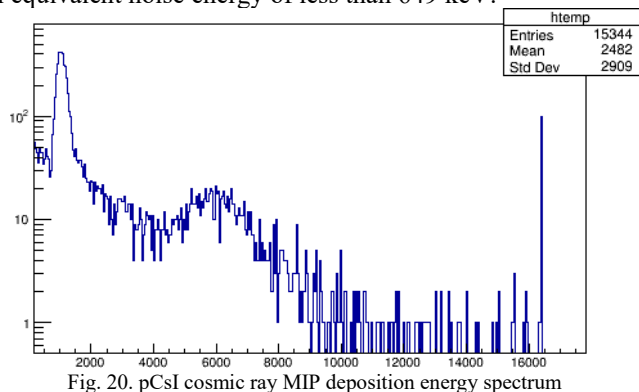

Fig. 20. pCsI cosmic ray MIP deposition energy spectrum

V. SUMMARY

In order to meet the needs of the STCF ECAL electronics for high-precision energy and time measurement, this paper studies and designs the readout electronic scheme proposes a low-noise and high-time-resolution readout scheme combined with the noise analysis of time and energy, and verifies the feasibility of the scheme, which provides a technical basis for the future development of STCF ECAL.

REFERENCES

[1] Luo, Q., and D. Xu. "Progress on preliminary conceptual study of HIEPA, a super tau-charm factory in China, talk at the 9th International Particle Accelerator Conference (IPAC 2018), held in Vancouver." British Columbia, Canada, April (2018).

[2] Abe, Tetsuo, et al. "Belle II technical design report." arXiv preprint arXiv:1011.0352 (2010).

[3] Boyarintsev, A., et al. "Study of radiation hardness of pure CsI crystals for Belle-II calorimeter." Journal of Instrumentation 11.03 (2016): P03013.

[4] Yang, Fan, Liyuan Zhang, and Ren-Yuan Zhu. "Gamma-ray induced radiation damage up to 340 Mrad in various scintillation crystals." IEEE Transactions on Nuclear Science 63.2 (2016): 612-619.

[5] Hamamatsu Photonics. Short wavelength type APD[EB/OL]. http://www.hamamatsu.com.cn/UserFiles/upload/file/20201210/s8664_series_kapd1012e.pdf.

[6] Hamamatsu Photonics. Si APD S8664-1010[EB/OL]. http://www.hamamatsu.com.cn/product/17018.html.

[7] Hamamatsu Photonics. Si APD S8664-55[EB/OL]. http://www.hamamatsu.com.cn/product/17140.html.

[8] Luo, Laifu, et al. "Design and optimization of the CSA-based readout electronics for STCF ECAL." Journal of Instrumentation 15.09 (2020): C09002.

[9] Achasov, M. N., et al. "SND electromagnetic calorimeter time measurement and its applications." Journal of Instrumentation 15.09 (2020): C09042.

[10] Luo, Laifu, et al. "Design and optimization of the CSA-based readout electronics for STCF ECAL." Journal of Instrumentation 15.09 (2020): C09002.

[11] Group T S S. STCF Conceptual Design Report Volume III - Detector, 2021.